Physica D 240 (2011) 363–375

Contents lists available at ScienceDirect

Physica D

journal homepage: www.elsevier.com/locate/physd

# Spatio-temporal chaos in a chemotaxis model

Kevin J. Painter [a,*], Thomas Hillen [b]

[a] Department of Mathematics and Maxwell Institute for Mathematical Sciences, Heriot-Watt University, Edinburgh, EH14 4AS, United Kingdom
[b] Centre for Mathematical Biology, Department of Mathematical and Statistical Sciences, University of Alberta, Edmonton T6G2G1, Canada

ARTICLE INFO

*Article history:*
Received 23 May 2010
Received in revised form
23 September 2010
Accepted 25 September 2010
Available online 1 October 2010
Communicated by B. Sandstede

*Keywords:*
Chemotaxis
Continuous models
Pattern formation
Spatio-temporal chaos
Morphogenesis

ABSTRACT

In this paper we explore the dynamics of a one-dimensional Keller–Segel type model for chemotaxis incorporating a logistic cell growth term. We demonstrate the capacity of the model to self-organise into multiple cellular aggregations which, according to position in parameter space, either form a stationary pattern or undergo a sustained spatio-temporal sequence of merging (two aggregations coalesce) and emerging (a new aggregation appears). This spatio-temporal patterning can be further subdivided into either a time-periodic or time-irregular fashion. Numerical explorations into the latter indicate a positive Lyapunov exponent (sensitive dependence to initial conditions) together with a rich bifurcation structure. In particular, we find stationary patterns that bifurcate onto a path of periodic patterns which, prior to the onset of spatio-temporal irregularity, undergo a "periodic-doubling" sequence. Based on these results and comparisons with other systems, we argue that the spatio-temporal irregularity observed here describes a form of spatio-temporal chaos. We discuss briefly our results in the context of previous applications of chemotaxis models, including tumour invasion, embryonic development and ecology.



## 1. Introduction

Movement plays a pivotal role in the arrangements of cells and organisms: within a developing embryo, coordinated migration allows nascent cells and tissues to rearrange and differentiate into adult structures; in populations of organisms, ordered flocks and shoals emerge via an individual altering movement with respect to a neighbour. Chemotaxis, the process in which cells (or organisms) migrate in response to external chemical gradients, has attracted significant interest. For certain bacterial populations, such as *Escherichia coli* and *Salmonella typhimurium*, it results in their arrangement into a variety of spatial patterns [1–3]. Via relay of the chemotactic agent cAMP, *Dictyostelium discoideum* aggregates from a population of individual cells into a multicellular and differentiated fruiting body (e.g. [4,5]). Within the embryo, chemotaxis plays a guiding role during avian gastrulation [6,7], pigmentation patterning [8] and neuronal development [9]. These same mechanisms are exploited during tumour growth, facilitating the invasion of cancerous cells into healthy tissue and driving angiogenesis.

While many models of chemotaxis have been formulated, the system of coupled partial differential equations introduced by Keller and Segel in [10] remains amongst the most widely utilised, its continuous nature enabling analytical tractability and straightforward integration with other models. We refer to [11] for a recent exploration of related classes of these equations. In this paper we explore the dynamical properties of the following specific form:

$$u_t = \nabla(D_u \nabla u - \chi u \nabla v) + f(u), \tag{1}$$

$$v_t = D_v \nabla^2 v + \alpha u - \beta v, \tag{2}$$

where $u(x,t)$ and $v(x,t)$ denote the cell density and chemoattractant concentration at time $t$ and location $x$. The above equations implicitly assume linear signalling kinetics, constant cell and chemical diffusion coefficients ($D_u$ and $D_v$ respectively) and a constant chemotactic sensitivity coefficient $\chi$. For the cellular growth term $f(u)$ we concentrate on the logistic form $f(u) = ru(1-u/K)$, where $r$ defines the growth rate and $K$ is the "carrying capacity".

Rescaling the equations such that

$$u^* = u/K, \qquad v^* = \frac{\beta}{\alpha K} v, \qquad t^* = \beta t, \qquad x^* = \sqrt{\frac{\beta}{D_v}}\, x,$$

$$D = \frac{D_u}{D_v}, \qquad \chi^* = \frac{\chi \alpha K}{\beta D_v}, \qquad r^* = \frac{r}{\beta},$$

yields (on dropping the *'s)

$$u_t = \nabla(D\nabla u - \chi u \nabla v) + ru(1-u), \tag{3}$$

$$v_t = \Delta v + u - v, \tag{4}$$

with the unique nontrivial uniform steady state at (1, 1). Hereafter we refer to $D$ as the cell diffusion coefficient, $\chi$ as the chemotactic coefficient and $r$ as the growth rate, although it is noted

* Corresponding author. Tel.: +44 0 131 4518234; fax: +44 0 131 4513249.
*E-mail addresses:* K.J.Painter@ma.hw.ac.uk (K.J. Painter), thillen@ualberta.ca (T. Hillen).

0167-2789/$ – see front matter © 2010 Elsevier B.V. All rights reserved.
doi:10.1016/j.physd.2010.09.011

that these are, in fact, nondimensional parameters that incorporate additional detail. In this paper we consider (3)–(4) on the one-dimensional interval $[0, L]$ and generally assume zero-flux (Neumann) boundary conditions. Boundary conditions can vary considerably according to the biological system, however zero-flux conditions are a pragmatic and natural choice in many applications, for example a population of bacteria cultivated in a petri-dish. Initial conditions, except where specifically stated, will take the form

$$(u(x, 0), v(x, 0)) = (1, 1 + \epsilon(x)), \tag{5}$$

where $\epsilon(x)$ is a small ($|\epsilon(x)| \leq 0.01$) spatially-varying random perturbation.

### 1.1. Paper outline

In this paper, we explore Eqs. (3)–(4) under cell growth ($r > 0$). We will use the remainder of this Introduction to review the relevant literature, describe the numerical scheme and briefly study the linear stability of the homogeneous steady state (1, 1). In Section 2 we review numerical and analytical results pertinent to the zero growth scenario, highlighting that while spatial pattern formation can occur, *multiple*-peak patterns are unstable and a coarsening process forms that leads (over long time scales) to a unique global aggregation. In Section 3 we show that inclusion of growth can lead to stable multiple aggregations, yet only for certain parameter regions. Other dynamics include a range of spatio-temporal patterning in which the pattern of aggregates evolves through alternating merging and emerging events in either time-periodic or arrhythmic fashion. Detailed numerical explorations of the latter reveal a positive Lyapunov exponent and sensitive dependence to initial conditions (Section 4). A numerical bifurcation analysis is developed (Section 5) to track how the solution class varies in parameter space. A bifurcation sequence was found in which increasing the chemotactic sensitivity first destabilises the uniform steady state and a stationary spatial pattern emerges. This, in turn, loses stability to spatio-temporal periodicity. As the chemotactic sensitivity increases further, a sequence of "period-doublings" occurs before the pattern degenerates into spatio-temporal irregularity. We conclude with a discussion of the results in the context of spatio-temporal chaos and specific applications.

### 1.2. Linear stability

Models of the form (3)–(4) are well known for their self-organising properties. Linearisation around the uniform steady state gives

$$U_t = DU_{xx} - \chi V_{xx} - rU,$$
$$V_t = V_{xx} + U - V,$$

for small perturbations $U(x, t), V(x, t)$. The stability of the homogeneous steady state is determined by the (temporal) eigenvalues of the stability matrix (e.g. see [12])

$$A_k = \begin{pmatrix} -Dk^2 - r & \chi k^2 \\ 1 & -k^2 - 1 \end{pmatrix}, \tag{6}$$

where $k \geq 0$ denotes the *wavenumber*: on the interval $[0, L]$ with zero-flux boundary conditions we have $k = n\pi/L, n = 0, 1, 2, \ldots$, where $n$ denotes the mode. If the stability matrix has at least one eigenvalue with a positive real part, the homogeneous steady state is unstable. A simple analysis reveals the following *necessary* condition for this to occur:

$$\chi > D + r + 2\sqrt{rD}. \tag{7}$$

The above relationship hints at the underlying mechanism that supports self-organisation: the positive feedback loop of chemotaxis-to and secretion-of the chemoattractant can overcome the stabilising properties of the growth and diffusive terms to round up an initially dispersed population into self-supported aggregations.

### 1.3. Previous literature and spatio-temporal properties

A substantial body of research exists on systems related to (1)–(2): we refer to [11] for a recent review. Here we comment on some specific results pertinent to the scenario in which both cell growth and chemotaxis are considered.

A series of articles by Murray and coauthors [13–16] have considered applications of Eqs. (1)–(2) (with the linear production of chemoattractant in Eq. (2) replaced with a saturating term, $\frac{\alpha u}{\mu+u}$) to processes of embryonic pattern formation, including pigmentation markings on snakes and alligator stripe patterns. A combination of stability, bifurcation and numerical analyses were employed to determine whether a chemotactic mechanism is capable of producing steady state patterns akin to those observed during development.

A number of studies have been undertaken on modelling spatial pattern formation in bacterial colonies (e.g. [3,17,18]). Typically, these models extend the simple cell—chemoattractant framework (1)–(2) to include an additional variable for a nutrient. Significantly, these models successfully generate much of the diversity of patterning observed in cultured bacterial colonies [1,2].

Applications of chemotaxis-based models have also been considered to model certain processes during tumour growth. Orme and Chaplain [19] employed a similar model to that of Murray and others above to understand the basis for capillary sprouting during tumour-induced angiogenesis. Chaplain and coauthors [20–22] developed a series of models to investigate tumour invasion processes. A detailed reaction–diffusion-taxis system was developed to describe the interactions between a proliferative and migratory tumour population, the surrounding extracellular matrix and various biochemical components involved in tumour-controlled matrix degradation. As the tumour cells invaded the surrounding tissue, a complicated and heterogeneous pattern of tumour cells was found to emerge in the wake of the invasive front.

Eqs. (1)–(2) and generalisations have also been studied mathematically [23–26]. Mimura [23] consider (1)–(2) on an unbounded domain $\mathbb{R}^n$, focusing on an Alee-like nonlinearity $f(u) = u(1 - u)(u - a)$. Here the kinetic term is bi-stable, leading to the splitting of the domain into distinct regions in which the solution is close to 0 and 1. A detailed asymptotic theory was developed for the evolution of the resulting boundary layers. The case studied in this paper is different, since the logistic form of $f(u)$ does not support such a phase separation. Osaki et al. [24] studied (3)–(4) on a two-dimensional bounded domain under homogeneous Neumann boundary conditions and the logistic form for $f(u)$. The existence of a compact global exponential attractor was proven, the subject for a more detailed study in [25]. There, lower estimates for the dimension of the corresponding finite dimensional exponential attractor were determined, showing that the dimension is at least the number of unstable eigenmodes of the linearisation at (1, 1). Later, we employ this estimate to compare the attractor dimension with the complexity of the patterns observed. Eqs. (3)–(4) have also been studied by Tello and Winkler [26], and Winkler [27], where the existence of unique global weak solutions is shown for sufficiently large $r$. In [27] it is suggested that Eqs. (3)–(4), in three dimensions and for sufficiently small $r$, may actually generate unbounded solutions, an interesting question for future study. Non-trivial steady states were also determined and it is shown that for $\chi < \frac{r}{2}$ all nontrivial solutions converge to the steady state (1, 1). Note that this condition is not satisfied under the assumption (7) for linear instability of the homogeneous solution. The conditions under which travelling wave solutions exist for Eqs. (1)–(2) has been the focus of a study in [28].

A range of studies have reported on the capacity of equations similar to (3)–(4) to exhibit a variety of spatio-temporal patterning processes, see Fig. 1 for a typical example. Painter and Hillen [29]

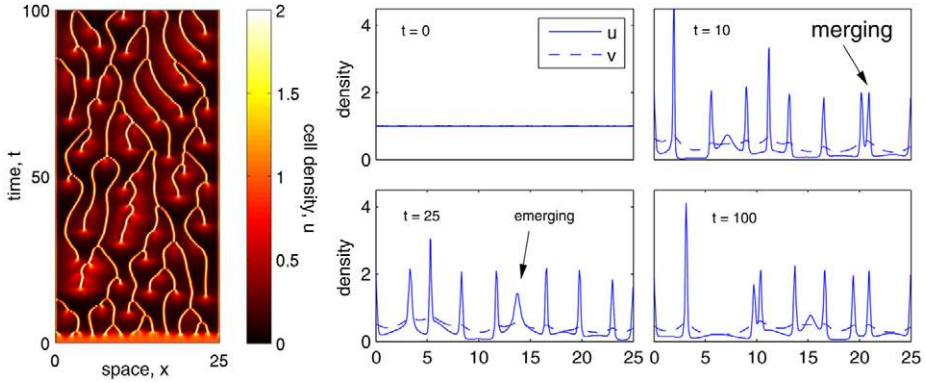


**Fig. 1.** An example of spatio-temporal patterning observed in Eqs. (3)–(4). Left: cell-density ($u$) plotted as a function of space (horizontal axis) and time (vertical axis). The colorscale bar indicates increasing cell density from $u = 0$ (black) to $u \geq 2$ (white). The uniform solution destabilises into a number of cellular aggregations which subsequently evolve through an apparently arrhythmic sequence of emerging and merging events. Right: four frames showing snapsots of the cell (solid line) and chemical (dashed line) distributions at the times indicated. Examples of merging and emerging events are indicated. For this set of simulations, Eqs. (3)–(4) are solved with $D = 0.1$, $r = 1.0$, $\chi = 5.0$ and $L = 25$ with initial conditions (5) and zero-flux boundary conditions. The numerical method is as described in Section 1.4, here we set $\Delta x = L/500$. A movie of this is available at http://www.ma.hw.ac.uk/~painter/research/chaos.html.

(see also [11]) explored a related version of (3)–(4), in which the chemotactic sensitivity is replaced with a "volume-filling" form. Inclusion of logistic cell growth was found to lead to a complex and (apparently) arrhythmic sequence of "merging and emerging" processes, in which the merging of two existing aggregates is interspersed with the emergence of a new peak. Aida et al. [25] study a typical bifurcation route for increasing chemotactic sensitivity in 2D. While small chemotactic sensitivities lead to asymptotically stable homogeneous steady states, moderate values generate stable non-homogeneous steady states. These become unstable to oscillations which, in turn, dissolve into an irregular pattern of merging and emerging local maxima at larger sensitivities. Wang and Hillen [30] have observed similar irregular merging–emerging dynamics in a model incorporating a nonlinear cell-diffusion term derived by allowing cells to squeeze into local openings.

This irregular spatio-temporal behaviour has also been observed for specific applications of chemotactic models. In the above described models for tumour invasion, Chaplain and Lolas [20,21] observed "anarchic" tumour cell populations that undergo irregular spatio-temporal behaviour in the wake of the invading front. Chemotaxis induced spatio-temporal patterning has also been observed in a model for host parasitoid interactions, see [31].

### 1.4. Numerical method

The numerical scheme adopts a Method of Lines approach in which the equations are first discretised in space on a uniform mesh (of spacing $\Delta x$), and the subsequent system of ODEs is then integrated in time. Discretisation of the diffusion terms is performed with a central differencing scheme, while the advective term is discretised using a high-order upwinding scheme with flux-limiting imposed to maintain positivity (e.g. see [32]). We use the ROWMAP stiff-systems integrator [33] to integrate the ODEs. Except where specified, we set error tolerances of $10^{-8}$ in ROWMAP. Verification of the scheme has been performed through varying $\Delta x$, error tolerances and using an independent (fully explicit) time-stepping scheme for a representative set of numerics. The qualitative behaviour of Eqs. (3)–(4) has also been independently confirmed using the MATLAB internal PDE solver (PDEPE).

## 2. Merging dynamics for chemotaxis models without cell-growth

We begin by briefly revisiting the zero growth scenario ($r = 0$), noting that this has been covered in much greater depth elsewhere (e.g. [11]). Typical numerical simulations for parameters that satisfy condition (7) are plotted in Fig. 2. Initially, Fig. 2(a), chemotaxis coupled with secretion of the attractant resolves the dispersed cell population into multiple aggregations. However, this same process generates additional dynamics on a logarithmic time scale, Fig. 2(b). Attraction between aggregates results in the gradual loss of mass from a smaller aggregate into a more dominant neighbour(s), and its eventual merging and/or collapse. As such, this coarsening results in the aggregates becoming more widely dispersed.

The merging process for $r = 0$ has been studied in detail by Schaaf [34], and for a related model in which $\chi$ is replaced by the density dependent form $\chi(1 - u/U_{\max})$ (see [29,35]). Potapov and Hillen [36] employed a numerical bifurcation analysis, indicating that merging corresponds to transient dynamics along metastable (multiple peak) steady states. Dolak and Schmeiser [37] utilised singular perturbation methods under a small diffusion approximation. In essence, two local maxima must be sufficiently close in order to "feel" each other and, hence, merge. This is reflected in a super-exponential time increase between merging events as the average distance between them increases (see Fig. 2(b)).

Biologically, this coalescence of chemotactic aggregations is observed in a number of real-life examples of chemotactic self-organisation, such as bacteria populations cultured in a liquid medium [1,2]. From a pattern formation standpoint, however, we are often interested in the robust generation of repeated structures: this is particularly pertinent to the emergence of certain embryonic forms, such as hair follicles, pigment patterns and somites, in which the pattern consists of multiple structures with a fixed (approximately) spatial wavelength. While the zero-growth model clearly generates these patterns *transiently*, it is unclear whether this would be sufficiently robust for such a context. Intuitively, cell growth could compensate any loss of cells from one aggregate to a neighbour.

## 3. Aggregation dynamics under cell growth

We consider $r > 0$ in Eq. (3). Following the nondimensionalisation, Eqs. (3)–(4) contain three unspecified parameters, $\chi$, $r$ and $D$, and the domain length $L$. Inevitably, determining estimates for such parameters would vary according to the biological system. For example, determining $D$ requires cell and chemical diffusion coefficients, yet estimates for the former can range between $2\text{–}4 \times 10^{-6}$ cm$^2$ s$^{-1}$ for *E. coli* cells in a liquid medium [38] and $O(10^{-10})$ cm$^2$ s$^{-1}$ for fibroblasts in an extracellular matrix [39].

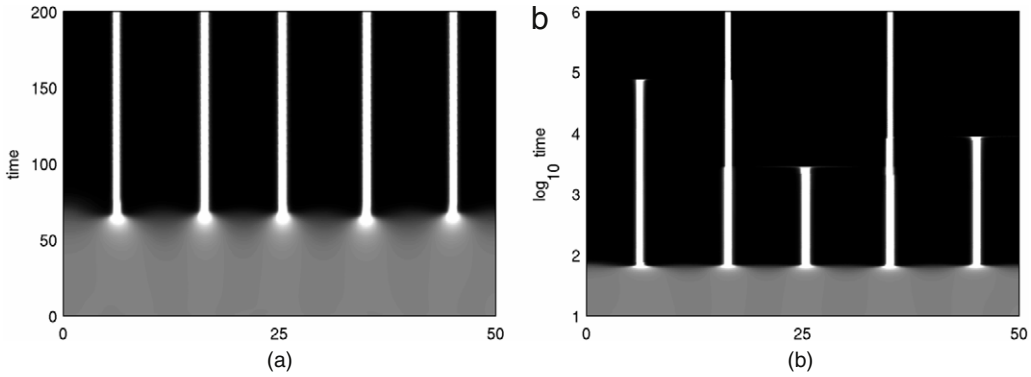


**Fig. 2.** Simulations of (3)–(4) with $r = 0$. Each plot tracks the space (horizontal axis)–time (vertical axis) cell density ($u$), with the grayscale reflecting an increasing cell density between $u = 0$ (black) and $u \geq 2$ (white). (a) Initial self-organisation of a homogeneously distributed cell population into distinct and (approximately) uniformly spaced aggregates. (b) Merging dynamics over a longer timescale. Competition between the aggregates leads to their gradual collapse, eventually resulting in a few widely dispersed aggregates. Eqs. (3)–(4) were solved with $D = 1$, $\chi = 2$, $r = 0$ and $L = 50$. Numerical method as in text with $\Delta x = L/500$.

Cell division rates are similarly variable, from as rapidly as once every 15 min or so (under appropriate nutrient conditions) for certain bacterial populations, to the orders of days and weeks in adult mammalian tissues. In the absence of a specific application and with the aim of a broader insight into the dynamical properties of the model we forego parameter determination. In the discussion we briefly consider the results in the context of specific applications.

Instead, we begin by performing repeated simulations of (3)–(4) under the initial conditions (5) on a fixed domain $L = 10.0$ with parameters $\chi$, $r$ and $D$ selected at random from uniform distributions in the following ranges:

$$0.01 \leq D \leq 2.0, \quad 0.0 \leq \chi \leq 20.0, \quad 0.0 \leq r \leq 2.0.$$

Eqs. (3)–(4) are computed until $t = T_{\text{end}}$ ($=10^4$) and the solution is classified at this time. Note that it is impossible to preclude slowly evolving transients, yet a representative subset of solutions computed to an extended time ($T_{\text{end}} = 10^5$) exhibited no significant change in the results. This initial analysis revealed that the long-time dynamics of solutions fall into multiple classes according to their spatio-temporal properties.

***H-solutions:*** **Homogeneous** steady state solutions. For parameter sets ($D$, $\chi$, $r$) that fail to satisfy (7), solutions quickly decay to the uniform state.

***S-solutions:*** **Stationary** spatial patterns. Multiple-peak patterns develop (see Fig. 3(a) I–V for typical examples) that do not undergo the merging dynamics associated with the zero-growth scenario.

***P-solutions:*** Spatio-temporal **periodic** solutions. Spatial aggregations develop that undergo sustained temporal interactions with a clear periodicity (see Fig. 3(b) I–V for various examples).

***I-solutions:*** Spatio-temporal **irregular** solutions. Spatial aggregations develop that undergo sustained temporal interactions with no discernible temporal periodicity (see Fig. 3(c) I–V for various examples).

The spatio-temporal behaviour can, on an intuitive level, be explained through the addition of growth to the merging behaviour discussed earlier: solutions evolve through a sequence of "merging" (as before) and "emerging" (in which new aggregations form). Briefly, the merging of existing aggregations via chemotactic attraction creates a "hole" in the patterning field. This space is then reoccupied via the emergence of a new aggregation peak driven by cell growth. Clarification into which pattern class a particular solution belongs can be obtained by tracking the $u$–$v$ phase-plane trajectories at discrete spatial locations. Typical trajectories for each of the above classes are plotted in the right hand column of Fig. 3: while H- and S-solutions simply correspond to fixed points, P-solutions correspond to closed orbits and I-solutions generate "strange attractor" type trajectories, as often associated with chaotic systems.

### 3.1. Variation within ($\chi$, $r$)-space

Our initial analysis revealed that the simple addition of cellular growth provides a mechanism for generating stationary multiple-peak patterns, yet the additional appearance of complex spatio-temporal behaviour raises further questions regarding their robustness. To explore this in greater detail, $D$ and $L$ are fixed and we explore dynamics at regularly spaced locations inside a portion of ($\chi$, $r$)-space. This creates small windows through which the variation in solution class across parameter space can be viewed. Fig. 4 summarises the results at two fixed pairs: (a) $D = 0.1, L = 10$, and (d) $D = 1.0, L = 20$. In these plots, H-solutions are denoted by a dot while P-solutions and I-solutions are represented by P and I respectively. For stationary patterns (S-solutions), we use a number to denote the total number of aggregates formed, where each internal aggregate is classified as 1 and each boundary aggregate is classified as 0.5. Note, therefore, that both the pattern of $n$-internal/2-boundary aggregates and that of $(n + 1)$-internal aggregates will be denoted by an "$n + 1$" in these plots.

Closer to the instability border (as determined by condition (7)), we predominantly observe stationary patterns, with the number of peaks varying with $r$. Deeper within the unstable region, however, spatio-temporal patterning becomes increasingly prevalent. This correlates with the 2D behaviour reported in [25], where increasing the chemotactic sensitivity resulted in a loss of stationary solutions and onset of spatio-temporal behaviour. We note that stationary solutions can be found throughout the parameter space, yet these become restricted to relatively narrow strips deeper inside the unstable region: in Fig. 4(d), regions of 3 and 4 stationary aggregates are separated by regions of P- and I-solutions. Analysis into spatio-temporal pattern evolution reveals the importance of parameters. Thus, the P-solution plotted in Fig. 4(b) (corresponding to the boxed location in Fig. 4(a)) switches between 1 and 2 aggregates, Fig. 4(c), while the I-solution in Fig. 4(e) (corresponding to the boxed point in Fig. 4(d)) varies between 3 and 4 aggregates. In both instances, this correlates with the position of the spatio-temporal pattern with respect to the surrounding S-solutions.

### 3.2. Variation with domain length

Above we showed that stationary patterns of distinct wavelength are typically separated by broad regions of spatio-temporal patterning. Within these regions, while the space between two existing aggregates permits new aggregate growth, proximity to a neighbour results in merging. This implies a role for domain size which we investigate by varying $L$ for two fixed parameter sets: (PS1) $(r, D, \chi) = (1, 1, 5)$ and (PS2) $(r, D, \chi) = (1, 1, 10)$. The former describes a point just inside the unstable region (as determined by condition (7)), and a plot of the dispersion relation for

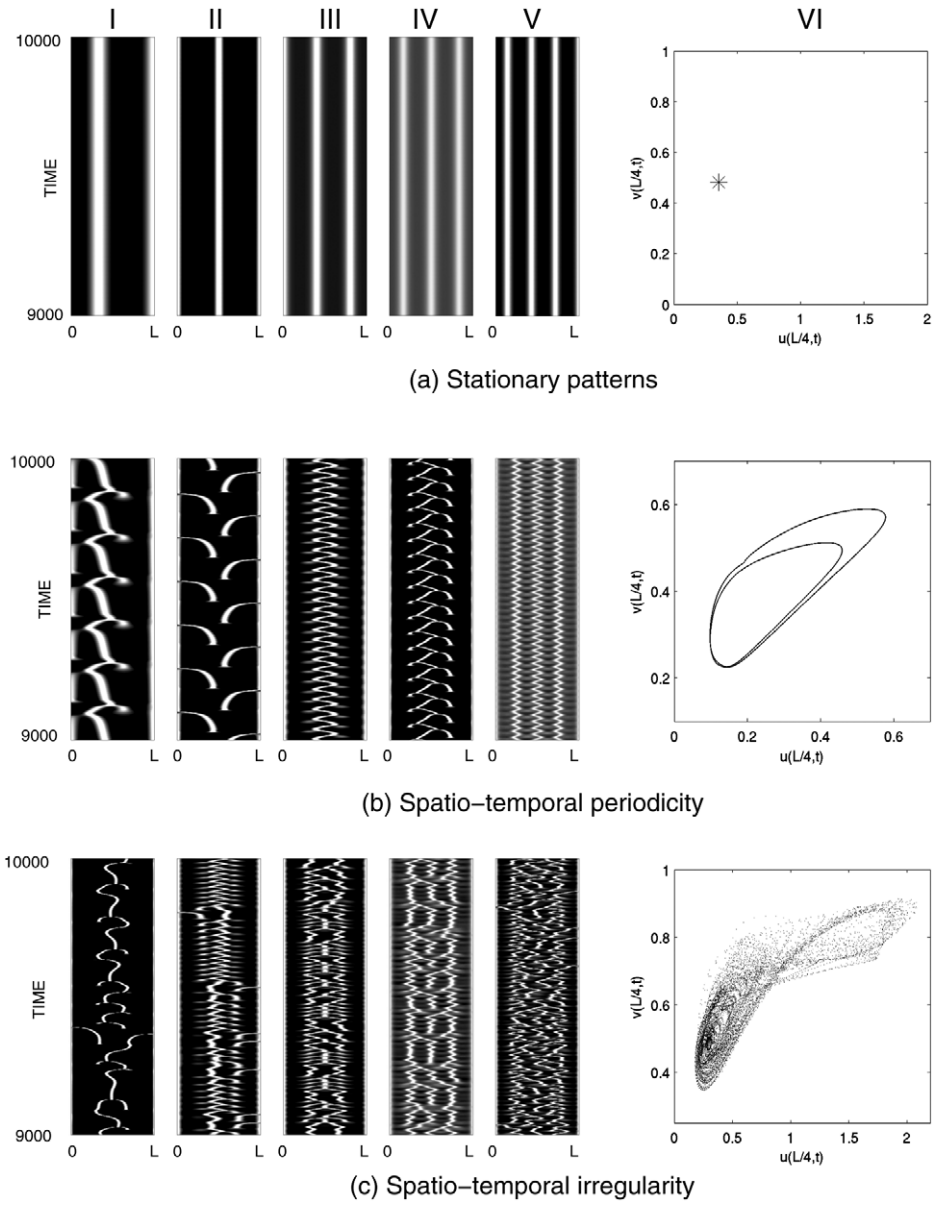


**Fig. 3.** Solution classes observed in Eqs. (3)–(4). In each row, columns I–V provide examples of each solution class: cell density ($u$) is plotted as a function of space (horizontal axis) and time (vertical) with the black to white grayscale reflecting an increasing cell density. Column VI plots a typical time trajectory in the $u$–$v$ phase plane at a specific spatial location (here, $x = L/4$). (a) Stationary patterns (S-solutions). Solutions evolve to a fixed spatial pattern with a characteristic spatial wavelength. The corresponding phase plane trajectory at $x = L/4$ yields a fixed point. (b) Spatio-temporal periodicity (P-solutions). Solutions evolve to a spatial pattern evolving with clear temporal periodicity. The corresponding phase plane trajectory gives a closed orbit. (c) Spatio-temporal irregularity (I-solutions). Solutions evolve to a spatial pattern evolving arrythmically. The corresponding phase plane trajectory at $x = L/4$ has a strange attractor appearance. For the simulations, the domain length was fixed at $L = 10$ while parameters $\chi$, $r$ and $D$ were randomly selected as described in the text. A total of 500 simulations were performed using the numerical scheme outlined in the text with $\Delta x = L/400$.

this set (Fig. 5(a), dashed line) reveals a correspondingly narrow range of unstable wavenumbers (i.e. for which at least one eigenvalue of the stability matrix (6) has positive real part). (PS2) defines a point within the unstable region, and the range of unstable wavenumbers is broader (solid line in Fig. 5 (a)). Under the imposed (zero-flux) boundary conditions, unstable wavenumbers are limited to the discrete values $k = \frac{n\pi}{L}$ for $n = 0, 1, 2\ldots$, where the mode $n$ indicates the number of aggregates ($n = 1$ corresponds to a single boundary aggregate, $n = 2$ corresponds to a full aggregate and so on). Thus, as $L$ is increased from zero, we expect the first pattern to become unstable to be a single boundary aggregate at some critical value $L_{\text{crit}}$. In Fig. 5 (b) we plot the unstable modes as a function of domain length under the two parameter sets; note the much wider range of unstable modes for (PS2).

We plot a representative subset for (PS1) in Fig. 6. Here, $L_{\text{crit}} = 1.94$ and there is a corresponding transition from H-solution to a 1-boundary aggregate S-solution as $L$ increases from 1 to 2. Further increases are accompanied by transitions in the number of aggregates in the spatial pattern that forms. For all explored domain lengths the patterns are of stationary type (S-solution).

With (PS2), $L_{\text{crit}} = 1.12$ and a similar bifurcation between H- and S-solutions occurs, see Fig. 7. At lower domain lengths, solutions are consistent with (PS1), with S-solutions evolving. However, as the domain length is steadily increased we observe a greater prevalence for spatio-temporal patterning, with a further tendency for I-solutions over P-solutions at larger domain lengths. A limited set of numerics performed at much larger domain lengths exclusively generated I-solutions (example shown for $L = 200$). As the domain length is increased, more and more modes become unstable, Fig. 5(b). This corresponds, according to Aida *et al.* [25], to an increase in the dimension of the attractor, and supports higher levels of complexity.

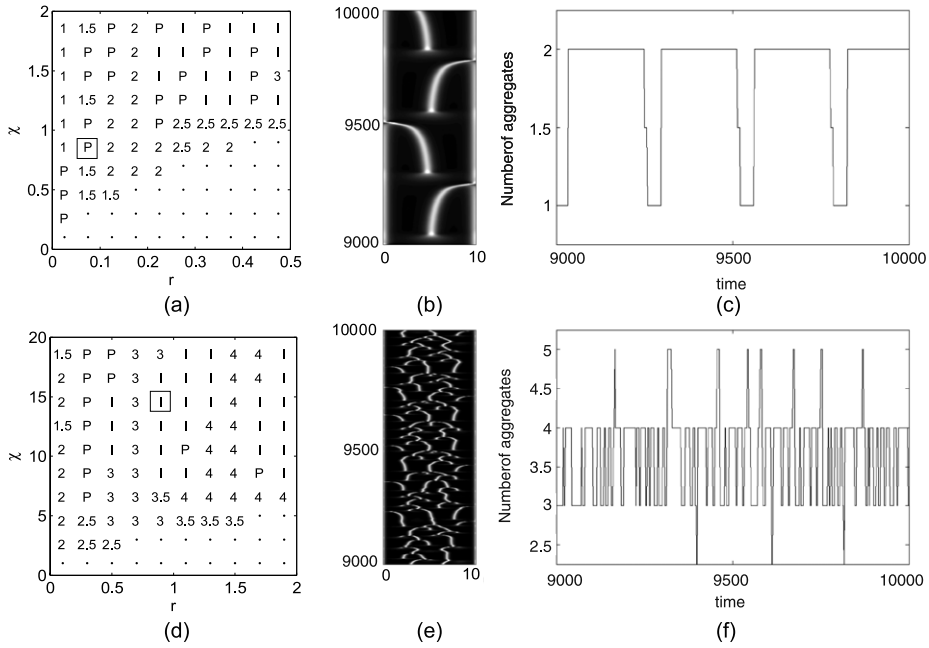


**Fig. 4.** (a) Variation in pattern class across $(r, \chi)$ parameter space when $D = 0.1$ and $L = 10$. Plot shows the pattern classified following a simulation of Eqs. (3)–(4) at various $(r, \chi)$ pairs: $(\cdot)$ H-solution; (Number) S-solution, with number indicating number of aggregates; (P) P-solution; (I) I-solution. (b) Space-time plot showing the cell density evolution for the P-solution found at the squared location in (a). (c) A plot of the number of aggregates as a function of time for the spatio-temporal pattern solution plotted in (b). (d)-(f) Equivalent set of results for $D = 1$ and $L = 20$. Numerics as described in the text, with $\Delta x = L/400$.

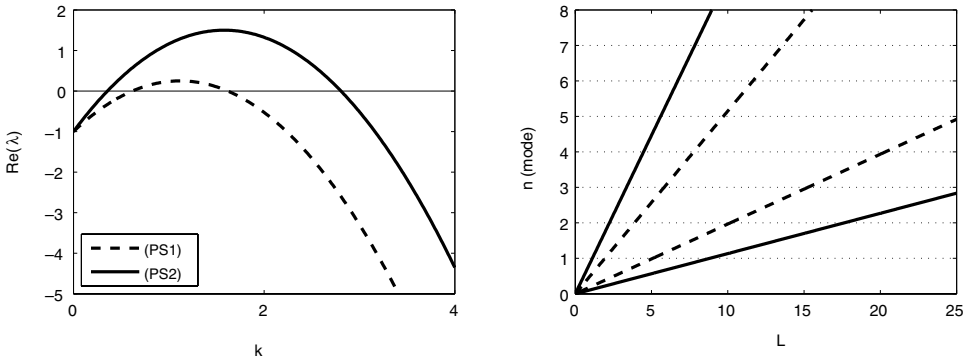


**Fig. 5.** (Left) Plot of the dispersion relation showing the range of unstable wavenumbers ($k$) for the two parameter sets (PS1) $(r, D, \chi) = (1, 1, 5)$ (dashed line) and (PS2) $(r, D, \chi) = (1, 1, 10)$ (solid line) for the numerical investigations. (Right) Plot showing the unstable modes as a function of domain length for each parameter set, using the same key as shown in the left hand plot.

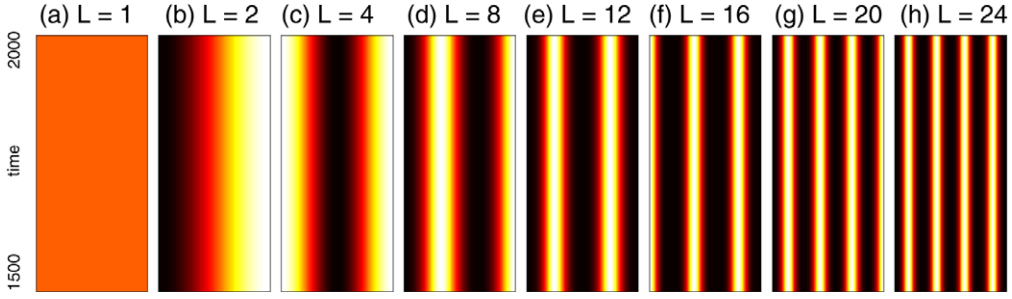


**Fig. 6.** Stationary patterns evolve close to the stability/instability interface over a range of domain lengths. Space (horizontal)–time (vertical) cell density maps for solutions to (3)–(4) with initial conditions (5) under varying $L$ and fixed $(r, D, \chi) = (1, 1, 5)$. Solutions are plotted for $t \in [1500, 2000]$ (note that a limited set of runs to larger times indicated no change in solution behaviour). The numerical method is as described in the text and we set $\Delta x = L/400$ (we note that the same qualitative behaviour was observed using the same fixed $\Delta x$ for each domain length).

### 3.2.1. Emerging length

The observation that new aggregates emerge as the domain length increases led us to investigate a possible "emerging length" $L_e$, i.e. a measure for the pattern transition between $L = 6$ and $L = 7$ in Fig. 7. For our argument we consider the space between two aggregates: here, the cell density is relatively low,

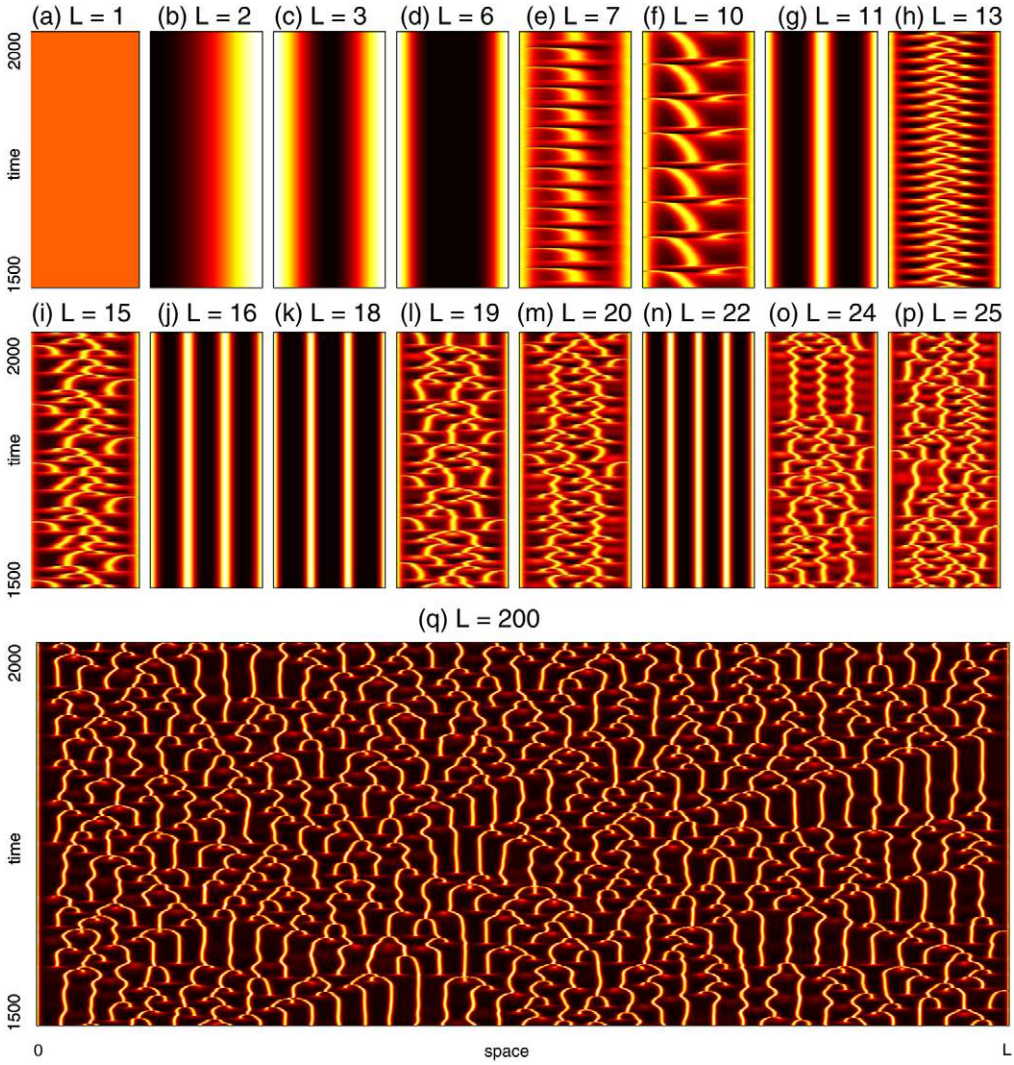


**Fig. 7.** A variety of H-, S-, P- and I-solutions are observed for (PS2) as the domain length is increased. Each frame shows the cell density ($u$) plotted in space (horizontal axis) and time (vertical axis) with the colorscale reflecting an increasing cell density between $u = 0$ (black) and $u \geq 2.0$ (white). Eqs. (3)–(4) were solved with $(r, D, \chi) = (1, 1, 10)$. Simulation details as in Fig. 6 for the top two rows. The same qualitative behaviour was also observed when using the same fixed $\Delta x$ at each domain length. For the bottom row (on a larger domain) we use $\Delta x = L/2000$.

increases in the population are predominantly driven by the proliferation term $ru(1-u)$ and newly created cells will be subject to both diffusion and chemotaxis. If a neighbouring aggregate is too close, the attraction may be sufficiently strong that new cells become absorbed into it before establishing their own. To form a separate and new aggregate, the local growth must overcome this attraction. At the onset of a new aggregate, at two locations between it and its neighbours the local flux will be zero and we therefore approximate an emerging length via a classical critical domain size problem in which the open space between aggregates must be large enough to support a non-constant population with zero flux boundary conditions, i.e.

$$\begin{aligned} u_t &= (Du_x - \chi u v_x)_x + ru(1-u), \\ v_t &= v_{xx} + u - v, \end{aligned} \tag{8}$$

on $[0, L_e]$ with boundary condition

$$u_x(0,t) = u_x(L_e,t) = 0, \qquad v_x(0,t) = v_x(L_e,t) = 0. \tag{9}$$

For the insertion of an additional aggregate in the interval $[0, L_e]$ the zero solution $(u^*, v^*) = (0,0)$ must be unstable. We use linearisation and find a corresponding eigenvalue $\lambda > 0$. To initiate an internal aggregate, the corresponding eigenfunction should have one isolated maximum in the middle of the domain. The linearisation of the above model (8) at $(0,0)$ reads

$$U_t = DU_{xx} + rU$$
$$V_t = V_{xx} + U - V.$$

The first equation decouples and can be studied separately: it is the same equation as for the standard critical domain size problem for the Fisher equation $u_t = Du_{xx} + ru(1-u)$ and the spectrum is well known (e.g. [40]). The eigenvalues are given by

$$\lambda_n = -D\left(\frac{n\pi}{L_e}\right)^2 + r, \quad n = 0, 1, 2, \ldots.$$

The first nontrivial eigenfunction with a maximum in the middle arises for $n = 2$. Hence the critical length for initiation of an internal maximum is given by

$$-D\left(\frac{2\pi}{L_e}\right)^2 + r = 0,$$

which can be solved by

$$L_e = 2\pi\sqrt{\frac{D}{r}}. \tag{10}$$

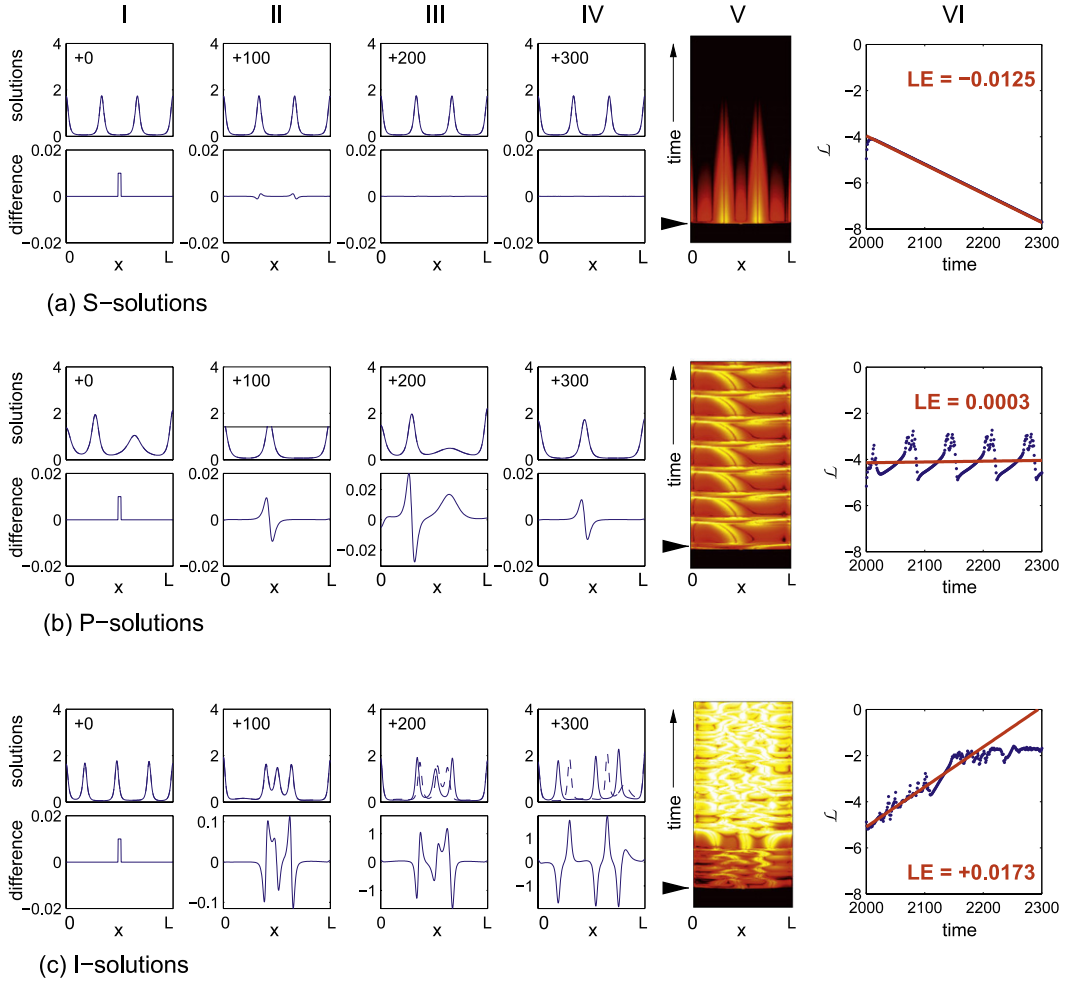


**Fig. 8.** Investigation into sensitive dependence to initial conditions for each pattern class. For each row, columns I–IV plot in the top subframe the solutions $u$ (solid line) and $u_{\text{pert}}$ (dashed line), and in the bottom subframe the difference $u - u_{\text{pert}}$ at distinct times: (I) immediately following the perturbation (+0), (II) 100 time units following the perturbation (+100), (III) +200 and (IV) +300. Column V plots the space–time density map for $\log_{10}|u_{\text{pert}}(x,t) - u(x,t)|$. The colorscale indicates levels between $\leq -6$ (black) and $\geq 0$ (white), and the arrowhead along the vertical axis indicates the time at which the perturbation is applied. Column VI gives the $\log_{10}$ plot of the absolute difference integrated over the domain length. In this plot we also draw the best-fit straight line (determined via least-squares method) following the initial perturbation. The slope of this line gives the numerical Lyaponov exponent (LE) as indicated. (a) S-solutions. Following the initial perturbation, the difference in solutions quickly decays to imperceptible levels. The numerical Lyaponov exponent is clearly negative. (b) P-solutions. Following the perturbation a slight phase shift occurs, indicated by the persistent (and periodic) difference in the solutions. The numerical Lyaponov exponent is effectively zero. (c) I-solutions. Following the perturbation, the difference between solutions grows over time. The numerical Lyaponov exponent is clearly positive. Numerical details and model parameter values as given in Fig. 7, with $T_{\text{pert}} = 2000$, $\delta = \varepsilon = 0.01$.

**Remarks:**

1. For Fig. 6, we note that $D = r = 1$ and $\chi = 10$, thus the emerging length is $L_e = 2\pi \approx 6.28$. Clearly, this corresponds with the switch between the S-solution at $L = 6$ and the emerging events at $L = 7$.
2. Note further that there is no dependence on $\chi$ in (10). Simulations similar to those in Fig. 6 with $D = r = 1$ (as above) and $\chi = 25$ demonstrate a similar transition from $L = 6$ to $L = 7$.
3. The emerging length also corresponds to the emerging distances observed for larger domain simulations.
4. Our emerging length estimate assumes that the flux vanishes at locations close to the existing peaks, reflected in boundary conditions (9). Under certain conditions this may not be satisfied, for example if the aggregates are diffuse, and the estimate may differ markedly from the actual emerging length.

## 4. Stability/robustness of solution classes

In this section we explore numerical stability for the various solution classes. To address this, we consider the impact of a small perturbation applied at $t = T_{\text{pert}}$ and track the subsequent difference between perturbed and unperturbed solutions. For the figures presented we consider a small step change to cell density applied to a central portion of the domain:

$$u_{\text{pert}}(x, T_{\text{pert}}) = u(x, T_{\text{pert}}) + \begin{cases} \varepsilon & \text{if } |x - L/2| \leq \delta L, \\ 0 & \text{otherwise,} \end{cases}$$

where $u_{\text{pert}}(x,t)$ and $u(x,t)$ are the perturbed and unperturbed solutions respectively, $\varepsilon$ is the size of the step and $\delta \in [0, 0.5]$ determines its width. Obviously, $u_{\text{pert}}(x,t) = u(x,t)$ for $t < T_{\text{pert}}$.

Fig. 8 plots typical results for (a) S-solutions, (b) P-solutions and (c) I-solutions. Columns I–IV plot in the top subframes the solutions $u(x)$ and $u_{\text{pert}}(x)$ at specific times following the perturbation, and in the bottom subframes the difference $u(x) - u_{\text{pert}}(x)$. In Column V we plot the base-10 logarithm of the absolute difference ($\log_{10}|u_{\text{pert}}(x,t) - u(x,t)|$) while in Column VI we plot the base-10 logarithm of the space-averaged absolute difference:

$$\mathcal{L}(t) = \log_{10}\left(\frac{1}{L}\int_0^L |u_{\text{pert}}(x,t) - u(x,t)|\,dx\right).$$

The slope of the best-fitting straight line (calculated via a least squares approximation) through $\mathcal{L}(t)$ following the perturbation

generates a numerical estimate for the Lyapunov exponent. Negative slopes indicate stability, zero-slopes imply neutral stability (for example, periodic orbits) and positive slopes indicate instability and a sensitive dependence to initial conditions (see [41]).

The results indicate that S-solutions are robust to perturbations: the perturbed solution quickly converges to the unperturbed solution, confirmed through a negative Lyapunov exponent. Periodic patterns remain periodic, yet a slight phase shift can be observed in the perturbed solution. Hence the error never decays to zero and the Lyapunov exponent is zero. I-solutions remain irregular and unperturbed/perturbed solutions diverge with time and $\mathcal{L}(t)$ increases towards a maximum, corresponding to the typical distance between arbitrary solutions. The straight line fitting to $\mathcal{L}(t)$ in the region where it is increasing yields a positive Lyapunov exponent, indicating sensitive dependence to the initial conditions. We note that the same tests have been applied for various examples in each class, for distinct forms and sizes of perturbations, and applied at different times ($T_{\text{pert}}$). In each case, equivalent behaviour was observed: I-solutions always generated a positive Lyaponov exponent, while P- and S-solutions generated zero and negative exponents, respectively.

## 5. Bifurcation path to spatio-temporal irregularity

In Section 3 we demonstrated that the parameter set significantly impacts on the class of patterning. Specifically, close to the stability/instability interface stationary solutions are predominantly observed, while further away spatio-temporal patterns can be found. In this section a more systematic analysis is conducted on the pattern class transition as we move through parameter space. Here we set $r = D = 1$ and $L = 20$ and vary the size of the chemotactic sensitivity $\chi$ in the following manner:

(i) set $\chi = 0$ and apply the initial conditions in (5);
(ii) Eqs. (3)–(4) are solved numerically until $T = T_{\text{end}}$ and the form of solutions is classified;
(iii) a small ($\leq$1%) spatially randomised perturbation is applied to the solution at $T = T_{\text{end}}$. This allows distinct branches originating at a particular bifurcation point to be tracked following multiple runs. The value for $\chi$ is incremented and we return to step (ii).

Thus, at each increment of $\chi$, a new simulation is initiated from the (perturbed) solution at the final time of the previous simulation (rather than random initial conditions). This approximates a continuous bifurcation analysis by tracking the changing (numerical) stability of specific solution branches as $\chi$ is increased. Switches between solution classes are interpreted as the loss of (local) stability for one branch and bifurcation onto a new one. We should stress that long-time transients cannot be excluded, yet identical results have been obtained in a more limited run with larger $T_{\text{end}}$. The above sequence was applied multiple times for the same parameter set with distinct randomised perturbations at $T_{\text{end}}$.

Under the fixed parameters $r = D = 1$, $L = 20$ and zero-flux boundary conditions, linear stability analysis predicts that the H-solution becomes unstable for $\chi > \chi^* \simeq 4.014$. Furthermore, for $\chi$ just above this value, we can expect growth of a 3 aggregate pattern, corresponding either to 2 internal/2 boundary peaks or 3 internal peaks. Under multiple runs of the simulation procedure, we observed two distinct sequences, summarised in Figs. 9 and 10, and corresponding to an initial bifurcation from H-solution to the 2 internal/2 boundary peak S-solution and 3 internal peak S-solution, respectively.

Fig. 9 describes the sequence in which the H-solution initially loses stability to a branch of 2-internal/2-boundary S-solutions as $\chi$ increases above $\chi^*$, see frames (a)–(b). This branch remains locally stable as $\chi$ is further increased, however peaks become notably sharper as the chemotactic attraction becomes stronger, Fig. 9(c). For $\chi \gtrsim 5.195$, however, the S-solution branch becomes unstable and a bifurcation is observed onto a path of P-solutions. Fig. 9(d) reveals this P-solution branch at $\chi = 5.21$: note that the oscillations begin small (reflected in a small closed orbit for the phase plane trajectories at $L/2$) but grow with further increases in $\chi$ (e.g. Fig. 9(e)).

Between $\chi = 5.275$ and $\chi = 5.28$ we observe a "period-doubling bifurcation" in the P-solution patterning class (compare Fig. 9(e) and (f)), classified by an increased spatio-temporal complexity and a doubling in the loop structure for the trajectories calculated at $x = L/2$. This period-doubling is also found to occur at other spatial locations at the same increment in $\chi$, although it is impossible to determine whether this is truly simultaneous across space: inevitably we are limited by the resolution in the numerical scheme. This new class of P-solution remains stable up to $\chi \sim 5.425$ before a second period doubling takes place (from 2-loop to 4-loop), c.f. Fig. 9(g) and (h). Small further increases in $\chi$ result in a loss of stability for P-solutions and a transition to I-solutions, determined by the appearance of trajectories at $x = L/2$, see Fig. 9(j)–(l). As $\chi$ is increased further, I-solutions remain, although it is noted that brief returns to P-solutions occur, for example, as shown in Fig. 9(m). The above "period-doubling" to irregularity sequence is commonly associated with chaotic systems.

An alternative sequence is found to take place when the initial bifurcation at $\chi^*$ results in the emergence of a 3-internal aggregates pattern, Fig. 10(a). This distinct S-solution branch subsequently loses stability to P-solutions at a lower value of $\chi$ than in the sequence represented in Fig. 9, as demonstrated in Fig. 10(a)–(b). We note that the closed orbits at $x = L/2$ first observed following the bifurcation from S-solutions to P-solution have a double-loop structure (i.e. there was no initial bifurcation into a single-loop orbit). As $\chi$ is increased further, P-solutions lose stability to I-solutions, Fig. 10(d)–(e). In this sequence, we also failed to observe the "period doubling" of the loop structure as above, although a possible explanation is an insufficient resolution for the step increase in $\chi$. With increasingly pronounced spatio-temporal irregularity, the density at one of the boundaries increases sufficiently to form a stable boundary aggregate and there is a switch from I-solutions to a 3.5 aggregate S-solutions for $\chi \gtrsim 5.13$. These two distinct bifurcation sequences clearly imply that multiple classes of solutions are locally stable at the same position in parameter space.

## 6. Discussion

The rich variety of patterning observed within even relatively simple models for chemotaxis is remarkable. To date, the majority of rigorous analysis has focused on finite time blow-up and/or global existence of solutions (e.g. [11,42] for reviews). While the existence of spatio-temporal patterning has been noted by a number of authors (e.g. [29,25,20,21,31,30,11]), a systematic analysis is currently lacking. In this paper we begin this study via a detailed numerical analysis of a basic chemotaxis model incorporating a logistic cell growth term, as given by (3)–(4). While we have not yet rigorously demonstrated chaotic behaviour, we have found both a positive Lyapunov exponent (sensitive dependence to initial conditions) and a potential period doubling route to spatio-temporal irregularity. Such features are often associated with chaotic systems, suggesting that Eqs. (3)–(4) are indeed capable of spatio-temporal chaos. We have also estimated the dimension of the compact global attractor using the results of [25], observing that increasing complexity correlates with growth in the attractor dimension. A full identification of the attractor would appear to be a highly challenging problem which we leave for future research.

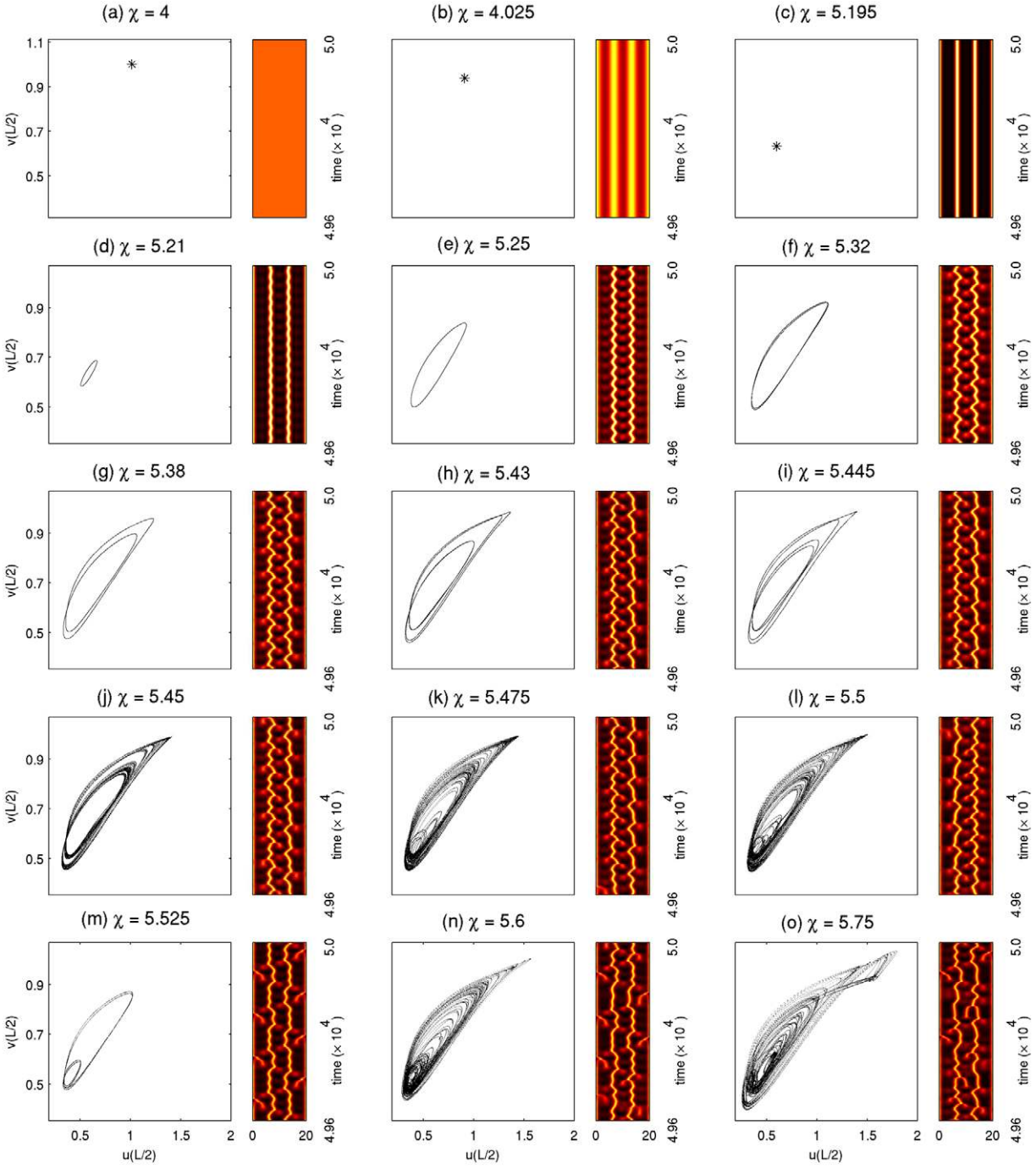


**Fig. 9.** Key transitions in solution class as the parameter $\chi$ is continuously increased, see text for details. For each subfigure (a)–(o) we plot (left) the $u$–$v$ phase plane trajectories for a specific spatial location ($x = L/2$) and (right) a portion of the space (horizontal axis)–time (vertical axis) cell density plot at the end of each simulation run. Numerical scheme as outlined in the text with other model parameters taken to be $r = D = 1$ and $L = 20$. We use $\Delta x = L/200$ for the spatial discretisation. A movie of this sequence is available at http://www.ma.hw.ac.uk/~painter/research/chaos.html.

Spatio-temporal patterning appears to occur via a repeating process of "emerging and merging" processes, in which a new aggregate emerges (driven predominantly by cellular growth) in a low density region of space before "merging" with existing aggregates (driven predominantly by chemotactic attraction). Interesting questions remain regarding suitable estimates for typical emerging lengths (the size of open space necessary for a new aggregate to develop) and merging lengths (i.e. a typical distance which leads to merging of peaks): relationships between these may determine whether stationary or spatio-temporal patterning occurs. In this paper we employed a simple stability analysis to estimate a value for the former, although it is noted that this estimate is imprecise under certain scenarios. For the latter, a number of perturbation arguments have been suggested in the literature (e.g. [36,37]), but thus far we have been unable to generate a critical merging size from these methods. The merging process observed here is reminiscent of coarsening dynamics in the Cahn–Hilliard equation [43].[1] In that case the coarsening process

[1] The literature on coarsening for Cahn–Hilliard equations and Ostwald ripening is immense. It is impossible to give due regard to all important contributions and we therefore confine ourselves to citing the original paper by Cahn and Hilliard to represent this large discipline.

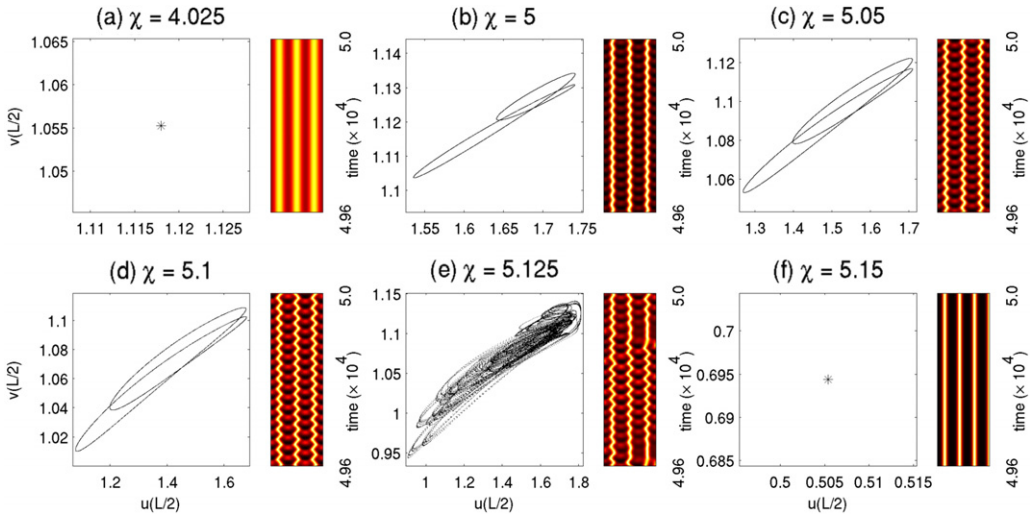


**Fig. 10.** Alternate bifurcation sequence to that presented in Fig. 9. Here, the initial transition from H- to S-solution results in a 3 internal aggregate pattern and the subsequent bifurcations are distinctly different. Model and numerical details as described in Fig. 9.

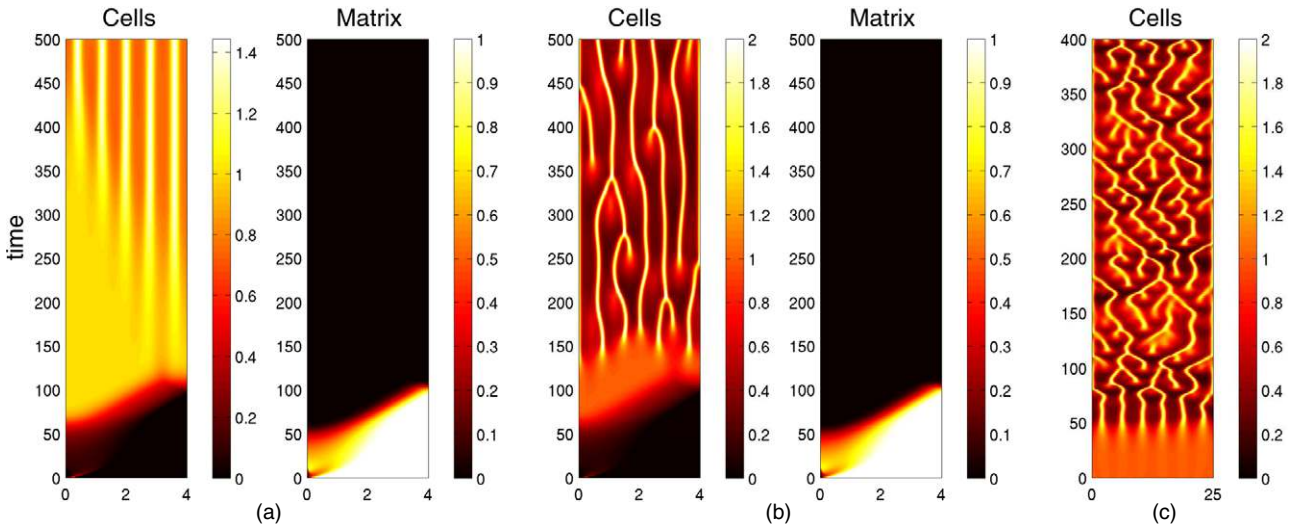


**Fig. 11.** Spatio-temporal patterning observed in specific applications of chemotaxis models similar to (1)–(2). (a), (b) Tumour invasion model of [20–22], see Eq. (11), showing space–time density maps for cells and the matrix. The initial invasion of the cells from left to right reduces the matrix to zero. The subsequent chemotactic interactions between cells and a proteolytic enzyme (not shown) generate both stationary and "anarchic" cell populations according to the size of the chemotactic sensitivity, consistent with the results in this paper. Equations as described in the text with $D_c = 0.001$, $D_p = 0.01$, $\phi = 0.05$, $\alpha = 0.1$, $\beta = 0.3$, $\delta = 5$, $\mu_1 = 0.15$, $\mu_2 = 0.75$ and (a) $\chi = 0.035$, (b) $\chi = 0.05$. Initially, we set a population of tumour cells at the $x = 0$ boundary and impose zero-flux boundary conditions on a domain of length $L = 4$. (c) Model for morphogenesis during embryonic development, in which the linear production of chemoattractant by cells in Eq. (2) is replaced by a saturating term $\frac{\alpha u}{\mu+u}$, see [14–16]. For sufficiently strong chemotaxis, the initially quasi-stationary pattern of cells degenerates into irregular spatio-temporal patterning. Parameter values are $D = 0.25$, $\chi = 10$, $r = \alpha = \mu = 1$ and $L = 25$. Initially we consider small randomised perturbations of the steady state and zero flux boundary conditions. Numerical method for all simulations as described in Section 1.4.

is driven by a double-well potential, which does not exist for the model studied here.

Closer inspection of the patterns reveals the complicated interactions between what appear to be travelling pulses and stationary local spikes. An exhaustive analysis into spike and travelling wave solutions of Eqs. (3)–(4), together with their stability properties, is an intriguing avenue for future research. Of ultimate interest is the geometric structure of the global attractor, the steady states and their unstable manifolds, which remains a distant goal.

The results presented here have been restricted to the case of zero-flux conditions applied at the boundary. While these are standard in many typical biological applications, it is important to remark that they can impose on the pattern form, particularly for smaller domains. To explore the potential impact of boundary conditions, a more restricted investigation was undertaken for periodic boundary conditions, and the same qualitative behaviour was observed. However, a more detailed exploration into the role of boundary conditions on the spatio-temporal properties of the model remains a subject for future research.

We also note the relevance of the results here in the context of certain applications. As mentioned earlier, Chaplain and coauthors [20–22] observed complicated spatio-temporal dynamics driven by chemotaxis in a detailed model for tumour invasion. A reduced version of their model, formulated in [21], considers the three equations:

$$\begin{aligned} c_t &= \nabla(D_c\nabla c - \chi c\nabla p - \phi\nabla m) + \mu_1 c(1-c-m),\\ m_t &= -\delta mp + \mu_2 m(1-c-m),\\ p_t &= D_p\nabla^2 p + \alpha c - \beta p. \end{aligned} \tag{11}$$

The above describes an invasive tumour cell population ($c$) which moves both haptotactically up gradients of the immobile extracellular matrix density ($m$) and chemotactically up gradients of a diffusible proteolytic enzyme ($p$). The latter is produced by the cells and degrades the extracellular matrix on contact. Cell proliferation and matrix regeneration are both modelled via logistic-type growth terms. The simulations plotted in Fig. 11(a)–(b) (using parameters and initial conditions from [21]) reveal how the initial wave of tumour cells invades through the tissue, leaving either stationary cell aggregates (Fig. 11(a)) or complicated spatio-temporal patterning (termed "anarchic" in [20–22], Fig. 11(b)) in its wake according to the size of the chemotactic sensitivity, $\chi$. Under the parameters indicated in the caption to Fig. 11, we note a scaling in which $\delta$ is large compared to other model parameters. Thus, $1/\delta$ is small and by dividing the second equation of (11) by $\delta$ we obtain $m \approx 0$ to leading order. In this case, Eq. (11) reduces to our model (1)–(2) and we can expect similar behaviour. Effectively, our chemotaxis model describes the outer solution on the slow manifold in a scaling limit of the Chaplain–Lolas model.

Models similar to Eqs. (1)–(2) have also been developed in the context of embryonic patterning [14–16] and angiogenesis [19]. Here, the linear production of chemoattractant by cells in Eq. (2) was replaced by a saturating term $\frac{\alpha u}{\mu+u}$, reflecting an additional feedback that curbs excessive attractant production at high cell densities. We note that irregular spatio-temporal patterning persists under this variation, see Fig. 11(c), as well as in other variations of the model (e.g. [29,30,11]).

In the context of embryonic development, this raises significant questions as to how robust basic cell-chemotaxis models would be for certain forms of morphogenesis: while it undoubtedly can generate stationary multi-peak patterns, the appearance of irregular spatio-temporal behaviour suggests an underlying sensitivity. Of course, we should note that developmental processes will be subjected to greater levels of signalling, additional patterning mechanisms, specific geometries, boundary constraints *etc.*, all of which may conspire to increase robustness.

A large amount of work has been conducted on irregular spatio-temporal patterning in ecological systems, see [44] for details. For example, Sherratt et al. [45] demonstrated the onset of chaotic oscillations in the wake of a predator population invading into a field of prey. Particularly pertinent to the present study on chemotaxis, Pearce et al. [31] have demonstrated chemotaxis-induced spatio-temporal irregularities in a host–parasitoid system. While the connection to the model developed here is less direct than the applications above, it is clearly tempting to speculate that a similar phenomenon of growth and chemotaxis may drive the dynamics reported in [31].

Although spatio-temporal chaos within a biological system has yet to be categorically demonstrated, the results here suggest that chemotactic processes offer a novel area for exploring the presence of such behaviour. The combined action of chemotaxis and growth has already been shown to drive complex spatial patterning in populations of cultivated bacteria (e.g. [1–3]), and the malleability of such systems offers a tantalising experimental case system for such investigations.

## Acknowledgements

We are indebted to Jonathan Sherratt (Heriot-Watt), Mark Chaplain (Dundee) and Alf Gerisch (Darmstadt) for a number of highly constructive comments and suggestions. KJP would like to acknowledge support from the Mathematical Biosciences Institute and BBSRC grant BB/D019621/1 for the Centre for Systems Biology at Edinburgh. TH would like to acknowledge support from NSERC.

## References

[1] E.O. Budrene, H.C. Berg, Complex patterns formed by motile cells of Escherichia coli, Nature 349 (1991) 630–633.
[2] E.O. Budrene, H.C. Berg, Dynamics of formation of symmetrical patterns by chemotactic bacteria, Nature 376 (1995) 49–53.
[3] D.E. Woodward, R. Tyson, M.R. Myerscough, J.D. Murray, E.O. Budrene, H.C. Berg, Spatio-temporal patterns generated by Salmonella typhimurium, Biophys. J. 68 (1995) 2181–2189.
[4] D. Dormann, C.J. Weijer, Chemotactic cell movement during Dictyostelium development and gastrulation, Curr. Opin. Genet. Dev. 16 (2006) 367–373.
[5] J.S. King, R.H. Insall, Chemotaxis: finding the way forward with Dictyostelium, Trends Cell Biol. 19 (2009) 523–530.
[6] X. Yang, D. Dormann, A.E. Munsterberg, C.J. Weijer, Cell movement patterns during gastrulation in the chick are controlled by positive and negative chemotaxis mediated by FGF4 and FGF8, Dev. Cell 3 (2002) 425–437.
[7] M. Chuai, C.J. Weijer, The mechanisms underlying primitive streak formation in the chick embryo, Curr. Top. Dev. Biol. 81 (2008) 135–156.
[8] V. Svetic, G.E. Hollway, S. Elworthy, T.R. Chipperfield, C. Davison, R.J. Adams, J.S. Eisen, P.W. Ingham, P.D. Currie, R.N. Kelsh, Sdf1a patterns zebrafish melanophores and links the somite and melanophore pattern defects in choker mutants, Development 134 (2007) 1011–1022.
[9] S.W. Moore, M. Tessier-Lavigne, T.E. Kennedy, Netrins and their receptors, Adv. Exp. Med. Biol. 621 (2007) 17–31.
[10] E.F. Keller, L.A. Segel, Initiation of slime mold aggregation viewed as an instability, J. Theoret. Biol. 26 (1970) 399–415.
[11] T. Hillen, K.J. Painter, A user's guide to PDE models for chemotaxis, J. Math. Biol. 58 (2009) 183–217.
[12] J.D. Murray, Mathematical Biology II: Spatial Models and Biochemical Applications, 3rd ed., Springer, New York, 2003.
[13] G.F. Oster, J.D. Murray, Pattern formation models and developmental constraints, J. Exp. Zool. 251 (1989) 186–202.
[14] J.D. Murray, M.R. Myerscough, Pigmentation pattern formation on snakes, J. Theoret. Biol. 149 (1991) 339–360.
[15] P.K. Maini, M.R. Myerscough, K.H. Winters, J.D. Murray, Bifurcating spatially heterogeneous solutions in a chemotaxis model for biological pattern generation, Bull. Math. Biol. 53 (1991) 701–719.
[16] M.R. Myerscough, P.K. Maini, K.J. Painter, Pattern formation in a generalized chemotactic model, Bull. Math. Biol. 60 (1998) 1–26.
[17] R. Tyson, S.R. Lubkin, J.D. Murray, A minimal mechanism for bacterial pattern formation, Proc. Biol. Sci. 266 (1999) 299–304.
[18] R. Tyson, S.R. Lubkin, J.D. Murray, Model and analysis of chemotactic bacterial patterns in a liquid medium, J. Math. Biol. 38 (1999) 359–375.
[19] M.E. Orme, M.A. Chaplain, A mathematical model of the first steps of tumour-related angiogenesis: capillary sprout formation and secondary branching, IMA J. Math. Appl. Med. Biol. 13 (1996) 73–98.
[20] M.A.J. Chaplain, G. Lolas, Mathematical modelling of cancer cell invasion of tissue: the role of the urokinase plasminogen activation system, Math. Modell. Methods. Appl. Sci. 15 (2005) 1685–1734.
[21] M.A.J. Chaplain, G. Lolas, Mathematical modelling of cancer invasion of tissue: dynamic heterogeneity, Netw. Heterog. Media 1 (2006) 399–439.
[22] V. Andasari, A. Gerisch, G. Lolas, A. South, M. Chaplain, Mathematical modeling of cancer cell invasion of tissue: Biological insight from mathematical analysis and computational simulation, J. Math. Biol. (2010). Online First doi:10.1007/s00285-010-0369-1.
[23] M. Mimura, T. Tsujikawa, Aggregation pattern dynamics in a chemotaxis model including growth, Physica A 230 (1996) 499–543.
[24] K. Osaki, T. Tsujikawa, A. Yagi, M. Mimura, Exponential attractor for a chemotaxis-growth system of equations, Nonlinear Anal. 51 (2002) 119–144.
[25] M. Aida, T. Tsujikawa, M. Efendiev, A. Yagi, M. Mimura, Lower estimate of the attractor dimension for a chemotaxis growth system, J. London Math. Soc. 74 (2006) 453–474.
[26] J.I. Tello, M. Winkler, A chemotaxis system with logistic source, Comm. PDE 32 (2007) 849–877.
[27] M. Winkler, Boundedness in the higher-dimensional parabolic-parabolic chemotaxis system with logistic source, Comm. PDEs 35 (2010) 1516–1537.
[28] G. Nadin, B. Perthame, L. Ryzhik, Traveling waves for the Keller-Segel system with Fisher birth terms, Interfaces Free Bound. 10 (2008) 517–538.
[29] K.J. Painter, T. Hillen, Volume-filling and quorum-sensing in models for chemosensitive movement, Can. Appl. Math. Quart. 10 (2002) 501–544.
[30] Z. Wang, T. Hillen, Pattern formation for a chemotaxis model with volume filling effects, Chaos 17 (2007) 037108.
[31] I.G. Pearce, M.A. Chaplain, P.G. Schofield, A.R. Anderson, S.F. Hubbard, Chemotaxis-induced spatio-temporal heterogeneity in multi-species host-parasitoid systems, J. Math. Biol. 55 (2007) 365–388.
[32] W. Hundsdorfer, J.G. Verwer, Numerical solution of time-dependent advection-diffusion-reaction equations, in: Springer Series in Comput. Math, vol. 33, Springer, 2003.
[33] R. Weiner, B.A. Schmitt, P.H., Rowmap—a row-code with Krylov techniques for large stiff odes, Appl. Numer. Math. 25 (1997) 303–319.
[34] R. Schaaf, Stationary solutions of chemotaxis systems, Trans. AMS 2 (1985) 531–536.
[35] T. Hillen, K. Painter, Global existence for a parabolic chemotaxis model with prevention of overcrowding, Adv. Appl. Math. 26 (2001) 280–301.
[36] A.B. Potapov, T. Hillen, Metastability in chemotaxis models, J. Dynam. Differential Equations 17 (2005) 293–330.

[37] Y. Dolak, C. Schmeiser, The Keller–Segel model with logistic sensitivity function and small diffusivity, SIAM J. Appl. Math. 66 (2005) 286–308.
[38] H.C. Berg, L. Turner, Chemotaxis of bacteria in glass capillary arrays. Escherichia coli, motility, microchannel plate, and light scattering, Biophys. J. 58 (1990) 919–930.
[39] V.H. Barocas, A.G. Moon, R.T. Tranquillo, The fibroblast-populated collagen microsphere assay of cell traction forcepart 2: measurement of the cell traction parameter, J. Biomech. Eng. 117 (1995) 161–170.
[40] G. de Vries, T. Hillen, M.A. Lewis, J. Müller, B. Schönfisch, A Course in Mathematical Biology, SIAM publishing, 2006.
[41] S.H. Strogatz, Nonlinear Dynamics And Chaos, Westview Press, 2000.
[42] D. Horstmann, From 1970 until present: the Keller–Segel model in chemotaxis and its consequences I, Jahresberichte DMV 105 (3) (2003) 103–165.
[43] J.W. Cahn, J.E. Hilliard, Free energy of a nonuniform system. I. interfacial energy, J. Chem. Phys 28 (1958) 258.
[44] H. Malchow, S.V. Petrovskii, E. Venturino, Spatiotemporal Patterns in Ecology and Epidemiology, Chapman and Hall, 2008.
[45] J.A. Sherratt, M.A. Lewis, A.C. Fowler, Ecological chaos in the wake of invasion, Proc. Natl. Acad. Sci. USA 92 (1995) 2524–2528.